Power Lever: To Transform Interlinking Architecture in Hybrid AC/DC Microgrids Community

Pengfeng Lin, *Member, IEEE*, Lingyu Du, *Graduate Student Member, IEEE*, Hongyi Zhang, *Graduate Student Member, IEEE*, Miao Zhu, *Senior Member, IEEE*, Jianjun Ma, *Member, IEEE*, and Peng Wang, *Fellow, IEEE*

***Abstract*—Microgrids (MGs) have shown considerable momentum in ongoing energy transition in global context. However, as the MGs progressively evolve into the configuration of MGs community, power congestion as well as complex power flow distribution inside hybrid ac/dc MGs community inevitably compromise efficient holistic system operations. Conventional approaches rely on interlinking converters to regulate power flow, but these systems operate under fully rated power schemes, leading to low efficiency and high cost. This article proposes a novel energy storage (ES)-based power lever (ES-PL), intending to transform the interlinking architecture of hybrid ac/dc MGs community. ES-PL is derived from a partial rated power scheme which gives rise to less power loss and saves system capital cost. By means of ES-PL, an interplexed global power sharing scheme is proposed to manipulate the power flow within the hybrid system such that entire system loads can be proportionally shared by all MGs. A complete dynamic model is carefully established, and the guidelines of key control parameter selection are presented based on comprehensive small signal stability analyses. The effectiveness of proposed ES-PL as well as its corresponding control strategy are verified by hardware experimentation.**

***Index Terms*—Hybrid ac/dc microgrids community, partially rated power scheme (PRPS), power lever, stability analysis.**

Received 6 April 2025; revised 26 August 2025; accepted 19 October 2025. This work was supported in part by the National Natural Science Foundation of China under Grant U2166216 and Grant 52507124 and in part by Shanghai Pujiang Talent Program under Grant 23PJ1405300. *(Corresponding author: Miao Zhu.)*

Pengfeng Lin, Lingyu Du, Hongyi Zhang, Miao Zhu, and Jianjun Ma are with Shanghai Jiao Tong University, Shanghai 200240, China (e-mail: pengfeng_lin@sjtu.edu.cn; dly848@sjtu.edu.cn; zhanghongyi@sjtu.edu.cn; miaozhu@sjtu.edu.cn; j.j.ma@sjtu.edu.cn).

Peng Wang is with Nanjing Normal University, Nanjing 210023, China (e-mail: epwang@ntu.edu.sg).

Digital Object Identifier 10.1109/TIE.2025.3629388

I. Introduction

A. Research Background

MICROGRIDS (MGs) have been proven to serve as key enabling technologies in modern smart grid systems, since they are able to integrate renewable energy sources in a more efficient and flexible way. On one hand, when the main grid is in faulty condition, MGs can be operated in a self-sustained manner wherein power generations match consumptions, and no electrical components would be affected by grid faults. On the other hand, as MGs normally incorporate various distributed energy resources (DERs), the surplus power induced in a localized MG can be fed back to the utility, given that the MG is properly linked to the main grid.

In global context, regulatory bodies are increasingly advocating for deregulation of electrical distribution systems. According to the database maintained by International Council on Large Electric Systems, DERs would now account for approximately 50% of distribution system capacity in highly developed cities [1]. These DERs are typically distributed across multiple MGs which are interconnected through a sophisticated network to form an MGs community. Within the community, heavily loaded MGs can receive power support from their peers, whereas the MGs with excess renewable productions would redistribute their surplus power without worrying about any possible over-voltage or -frequency issues. In this way, a multilateral energy exchange can be ensured by interconnected architecture which escalates overall system reliability and efficiency [2].

B. Literature Review

Note that an MGs community contains a plethora of MGs that could be interconnected in series, parallel, or complex way. In fact, a hybrid MGs community has been running in Semakau Island, Singapore, for over 5 years [3]. In an MGs community, arbitrary two autonomous MGs would be linked either by a simple power line or an interlinking converter (ILC). For the former case, the power flow over the line is naturally determined by the bus voltage difference between the two MGs, and each bus voltage is determined by a local controller [4], [5], [6]. For the case where ILC is adopted, the power exchange between the

MGs at the two ends of ILC can be easily manipulated. From the perspective of the entire MGs community, ILC helps to shift the power flow from overloaded lines to underused corridors, avoiding energy transfer congestion and ensuring power flow safety at the system level [7]. In typical hybrid ac/dc MG research area, an ILC is normally used to bridge ac and dc subgrids. A normalization approach is proposed in [8] to uniformly map floating dc voltage and ac frequency into the same range, such that the two different electrical quantities could be comparable. Then the power reference of the ILC can be generated to balance the load conditions of each subgrid. In [4], a multiparalleled ILC structure is explored and commissioned to realize bidirectional power transfer between ac and dc subgrids. The total power exchange is proportionally shared by all ILCs based on their respective ratings. A uniform control particularly designed for ILC is presented in [9] to achieve smooth ILC mode transitions. When all of the main power sources in a subgrid are down, the control strategy can immediately channel the energy from the other normal subgrid to power up the affected loads. A distributed control is then applied to manage the power flow over ILCs connected in parallel, and the uniform control is retained to attain hybrid system resilience, as reported in [10].

Although ILCs and the corresponding control in above literature have been working commendably in power flow regulations, the aforementioned ILCs could be all classified as fully rated power scheme (FRPS), which has been widely demonstrated being less efficient and induced higher capital cost than those facilities developed upon partially rated power scheme (PRPS) [11], [12], [13], [14]. As shown in Fig. 1, the ILC designed based on FRPS is connected in parallel with the MGs residing on its two ends. It is then expected to deal with the full power interactions between two MGs. In this sense, it is easy to comprehend that FRPS-enabled ILCs are required to be sized subjected to full bus voltage range and the highest current that may take place in actual operations. In contrast, the converter derived from PRPS is connected in series with a power line, which handles a small portion of power interactions without effecting the intended power exchange between two specified MGs. The current flowing through the converter is the power line current (see in Fig. 1), whereas the voltage across the converter is merely the voltage difference between two MG buses, which accounts for merely a small portion of rated MG system voltage. Hence, the power rating of PRPS-enabled converter is much smaller than that of FRPS based ones. As understood from [15], the power switches designed for high voltage applications inherently possess higher on-resistance, resulting in increased conduction loss and lesser working efficiencies. Therefore, it is safe to conclude that PRPS-based converter design would definitely outperform existing FRPS-based ILCs, offering more cost-effective solutions to system-level power flow regulations in hybrid ac/dc MGs community.

In dc transmission/distribution systems, there are emerging research outcomes reporting how to leverage PRPS to design converters for complex power flow controls. PRPS is applied to configure a two-line dc power flow controller (DCPFC) in [16], where several H-bridge modules are stacked up to enable power interactions between two transmission lines. In [17], the power shifting capability of DCPFC is extended and the power flow can be budged between three lines. The DCPFC presented in [17] features modularity, which means it is also applicable to the system necessitating power flow translations among four or more lines. Similar efforts can also be found in [18] and [19], respectively, where dual active bridge modules are utilized to bridge two transmission lines [18] and a nonisolated four-switch converter integrated with coupled inductors is adopted for power flow management [19]. Another type of modular interline power flow controller is reported in [20] and [21], where multiple full- or half-bridge-based modules are connected in series and embedded into a meshed multiport dc transmission system. Nevertheless, it is necessary to pinpoint that all the above methods could only achieve a "zero-sum" redistribution of power flows across various power lines. In any condition, there must be at least one line for which power flow cannot be regulated, as it should work as a slack line to ensure power flow distribution balance [22]. This resembles a characteristic in bulk power systems: when addressing the load flow calculations, a slack bus must be carefully defined to compensate for any possible disparity between generation and consumption [23]. The existence of "zero-sum" scheme would unnecessarily result in the lack of control degree of freedom (CDoF), thus possibly undermining system flexibility and economic operations.

C. Research Gap and Contributions

An MGs community has ac MGs and dc MGs interlinked by a sophisticated impedance network. To the best of author's knowledge, almost all ILCs that work on power flow regulations in hybrid ac/dc MGs community are designed based on FRPS. As explained earlier, the converters derived from FRPS are less efficient and costlier than those from PRPS. It is thus highly imperative to design a PRPS-enabled power conversion facility to thoroughly transform the interlinking architecture throughout MGs community, such that the power flow over the impedance network can be manipulated more flexibly and the whole operational cost can be considerably saved. In this article, a novel energy storage (ES)-based power lever (ES-PL) that serves as a brand-new approach to transform the interlinking architecture of hybrid ac/dc MGs community is proposed. The proposed ES-PL aims to provide brand-new insights for the next generation hybrid ac/dc MGs community with higher operational efficiency and flexibility, where interlinking architectures among different MGs can be delicately transformed by the proposed ES-PL. Not only does ES-PL inherit the advantage of PRPS that gives rise to much more cost-effective facility design, but it also, benefiting from the consolidation of ES system, breaks the aforementioned "zero-sum" limitation of conventional DCPFCs. Fig. 1 shows the comparison between two architectures (ES-PL by PRPS and ILCs by FRPS). ILCs can only be embedded into the power pathway between two specific MGs (i.e., MG_3-MG_2 and MG_3-MG_4, respectively), whereas ES-PL is positioned near MG_1 to interconnect two power lines branching out to MG_2 and MG_7, then to actively coordinate the power flows of two lines. Without loss of generality, interline power flow control can also be realized in the case that

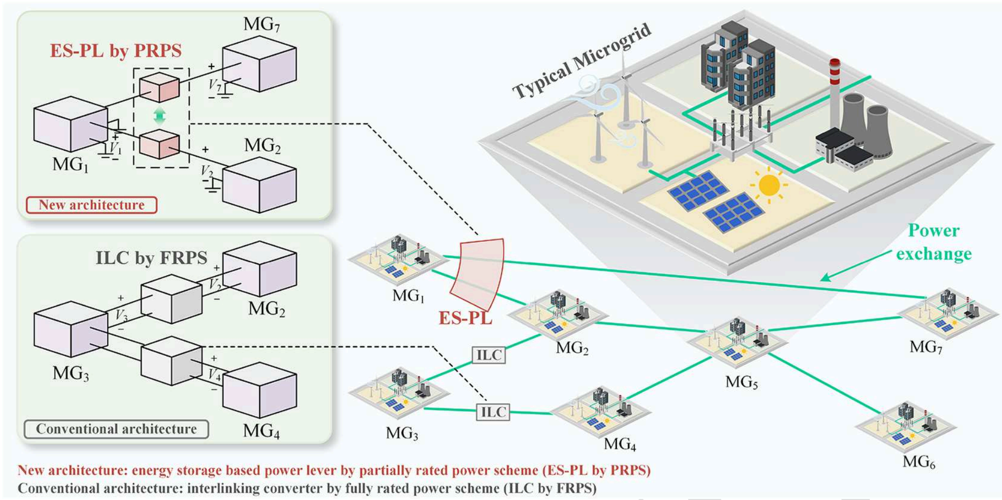

Fig. 1. Comparison between the proposed ES-PL and ILCs. ES-PL is constructed on two monopolar positive lines, while ILCs need to interconnect two MGs via both positive and negative lines.

three or more power lines are linked by the proposed ES-PL. Key contributions of this article are summarized as follows.

1) An ES-PL configuration is proposed. By its name, ES-PL indicates that, the regulation of a large portion of power flow can be realized by merely manipulating a small portion of power from ES, which is akin to the widely known leverage effect, as seen in Fig. 2. ES is widely recognized as a critical technology for enhancing system flexibility in modern power systems with high renewable energy penetration [24]. However, existing research predominantly focuses on deploying ESs in parallel configurations (either on the generation or end-user side) to improve flexibility. In contrast, the series connection of ES into impedance networks remains largely unexplored. The proposed ES-PL design introduces a highly modular structure that includes an additional port for the ES integration. This series-connected ES requires a much smaller rating than the parallel-connected counterpart, which typically requires rating sizing comparable to the system power level [25]. Meanwhile, the integration of ES provides an extra CDoF compared to traditional power flow controllers, enabling the ES-PL to actively participate in interline power flow regulations and significantly enhancing system operational flexibility.
2) An interplexed global power sharing (GPS) control scheme is proposed particularly for the ES-PL incorporated within a hybrid ac/dc MGs community. As shown in Fig. 3, the community system has three dc MGs and an ac MG and the system is operated in islanded mode [26]. The ac MG offers a dc terminal which can be consolidated into a dc impedance network. Different from typical FRPS-based ILCs which provincially concentrate on their designated power flow pathways, ES-PL exhibits sophisticated interior dynamic couplings among multiple power lines, which endows more efficient power flow translations. The proposed interplexed GPS control leverages on the multimode operations of ES-PL and MGs' individual droop characteristics to realize cross-channel control signal interplex. This ensures that all loads in the hybrid system can be shared among MGs in proportion to their respective ratings.
3) Full state-space model of a hybrid ac/dc MGs community equipped with ES-PL is formed, and the key control parameter selection guideline is presented. The model is a comprehensive small-signal model that captures the complete dynamics of droop-controlled ac/dc MGs, dc impedance network, and ES-PL. On one hand, a system of multivariable nonlinear algebraic equations is defined to find out power flow solutions to the hybrid community at various loading conditions. On the other hand, the linearized full state-space model helps to determine the existence of each operating equilibrium and also to identify the allowable variation range of proportional-integral (PI) parameters in the proposed interplexed GPS scheme. Then the parameters can be tuned by conducting comparative time-domain simulations.
4) The proposed ES-PL by PRPS demonstrates the dual advantages over conventional ILCs by FRPS in terms of capital cost and converter loss across the full operational range. Specifically, enabled by the use of lower-voltage-tolerance components, it achieves less conduction loss. Moreover, the PRPS mechanism significantly lowers capital cost compared with ILC implementations by reducing the required converter power capacity while maintaining the same power flow handling capabilities. These cost and loss advantages are quantitatively validated over a wide range of operating points against different loading conditions in ac and dc MGs.

Following the introduction in Section I, Section II illustrates the proposed ES-PL and its electrical characterization. Section III analyzes the proposed interplexed GPS scheme for a networked hybrid ac/dc MGs community. In Section IV, a linearized small-signal model is established to study the system stability and the selection guideline of key parameters is presented. Section V elaborates on the advantages of the proposed ES-PL. In Section VI, the feasibility of ES-PL and GPS scheme

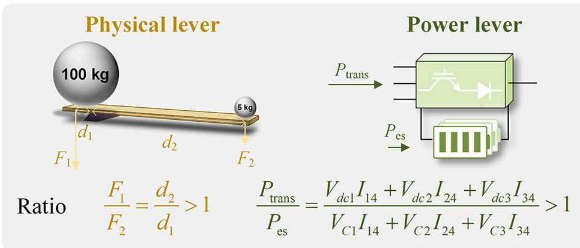

Fig. 2. Analogy between physical lever and power lever.

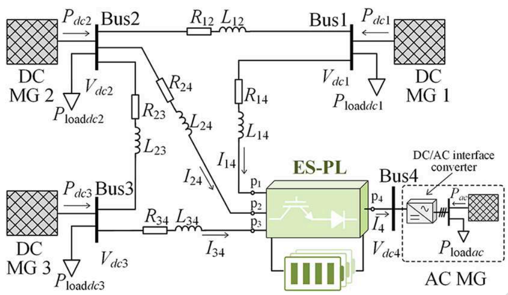

Fig. 3. Hybrid ac/dc MGs community with a dc impedance network incorporated with the proposed ES-PL.

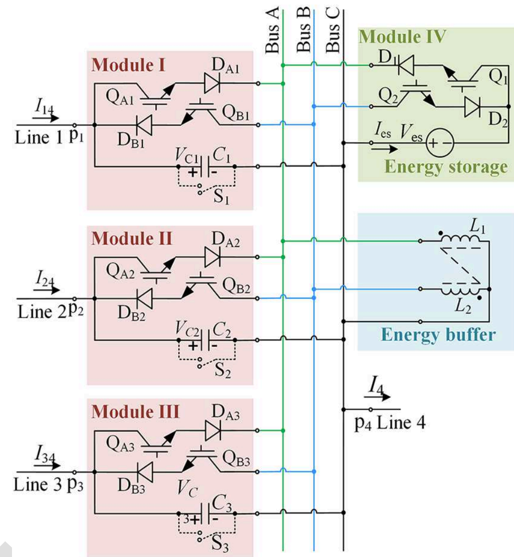

Fig. 4. System configuration of the proposed ES-PL.

is verified by hardware experimentation. Finally, Section VII concludes this article.

II. Proposed ES-PL

A. ES-PL System Configuration

Fig. 4 shows the system configuration of the proposed ES-PL. It is characterized by modularized design and high scalability. ES-PL in Fig. 4 can be applied to a hybrid system comprising three dc MGs and one ac MG as shown in Fig. 3. On the left-hand side, it connects to three lines (lines 1, 2, and 3) from the dc MGs, while line 4 extends to couple with ac MG. From a system configuration perspective, ES-PL contains five modules: modules I–IV and an energy buffer. All these modules are cross-coupled via buses A, B, and C. Module (I–III) contains a capacitor (C_1, C_2, C_3) connected in parallel with a circuit breaker S_i, which allows for commission and decommission of the module. The diodes (D_{A1}–D_{B1}, D_{A2}–D_{B2}, D_{A3}–D_{B3}) are arranged in an anti-parallel positions with their corresponding switching devices (Q_{A1}–Q_{B1}, Q_{A2}–Q_{B2}, Q_{A3}–Q_{B3}), forming bidirectional power flow paths between the input lines and the corresponding internal buses. This switching configuration enables bidirectional current conduction for different operating conditions. Taking module I of the ES-PL as an example, when I_{14} flows in the same direction as the reference direction (in Fig. 4), Q_{A1} and D_{A1} are activated. They work together with L_1 to form a loop such that the energy exchange between the inductor and the capacitor in module I can take place, through bus A. Conversely, when I_{14} flows in the opposite direction to the reference direction, Q_{B1} and D_{B1} are activated. They work together with L_2 to form a loop such that the energy exchange between the inductor and the capacitor in module I can take place, through bus B. It is the co-existence of two sets of IGBT-diode pairs, bus A, and bus B that enables the bidirectional power flow on line 1 (or module I). In module IV, by using the same power device structure as other modules, the ES replaces capacitor to constitute an ES port. When it comes the case where more power lines need to be integrated into ES-PL, the same module can be added without any modifications. The coupled inductors are used as an energy buffer to facilitate the power interactions within ES-PL. For Modules I–III, there are two modes. **AQ4**

1) Mode 1: When Q_{Ai} is turned on and Q_{Bi} is turned off, C_i is connected to bus A and bus C. Energy is transferred from C_i to the energy buffer.
2) Mode 2: When Q_{Bi} is turned on and Q_{Ai} is turned on, C_i is connected to bus A and bus C. Energy is transferred from the energy buffer to C_i.

ES is integrated into ES-PL by module IV. Its three operational modes can be summarized as follows.

1) Mode 1: Q_1 is turned on, and Q_2 is turned off. The ES absorbs excess energy from the system.
2) Mode 2: Q_1 is turned off, and Q_2 is turned on. The ES compensates for the energy deficit in the system.
3) Mode 3: Q_1 is turned off, and Q_2 is turned off. The ES is bypassed.

In modes 1 and 2, ES adds an additional CDoF to the system. The following is an example of the operating condition of ES-PL in a scenario where I_1, I_2, and I_3 are aligned with the reference direction as stipulated in Fig. 4. In this case, the ES absorbs energy from the three lines. The complete switching cycle can be divided into four substates.

1) Substate 1: Q_{A1} is turned on, and Q_{B1}, Q_{A2}, Q_{B2}, Q_{A3}, Q_{B3}, Q_1, Q_2 are turned off. During this time, energy is transferring from C_1 to L_1.
2) Substate 2: Q_{A2} is turned on, and Q_{A1}, Q_{B1}, Q_{B2}, Q_{A3}, Q_{B3}, Q_1, Q_2 are turned off. During this time, energy is transferring from C_2 to L_1.

3) Substate 3: Q_{A3} is turned on, and Q_{A1}, Q_{B1}, Q_{A2}, Q_{B2}, Q_{B3}, Q_1, Q_2 are turned off. During this time, energy is transferring from C_3 to L_1.
4) Substate 4: Q_1 is turned on, and Q_{A1}, Q_{B1}, Q_{A2}, Q_{B2}, Q_{A3}, Q_{B3}, Q_2 are turned off. During this time, energy is transferring from L_1 to ES.

The proposed ES-PL features a modular topology structure. The device presented in this article connects three dc MGs and one ac MG. The proposed ES-PL can be applied to simpler systems by reducing the number of modules.

B. ES-PL Electrical Characterization and Power Leverage Ratio

As a brand-new power flow manipulation infrastructure expected to transform the dc interlinking architecture of hybrid ac/dc MGs community, similar to all other types of devices in power grids, the electrical characterization of ES-PL should be given.

Take the operating condition in Section II-A as an example. Set the duty cycle of Q_{A1}, Q_{A2}, Q_{A3}, and Q_1 as d_1, d_2, d_3, and d_4, which satisfy the following expression:

$$d_1 + d_2 + d_3 + d_4 = 1. \tag{1}$$

According to volt-second balance principle of inductor, the integral of inductor's current should be zero during a switching cycle

$$(V_{C1}d_1 + V_{C2}d_2 + V_{C3}d_3 - V_{\text{es}}d_4)T_s = 0 \tag{2}$$

where T_s is the switching cycle of ES-PL.

Similarly, according to the principle of capacitor charge balance principle, the voltages of C_i should be continuous, then the following expression holds:

$$(I_{i4} - I_L)d_iT_s + I_{i4}(1 - d_i)T_s = 0 \tag{3}$$

where I_{i4} is the current of line i, and I_L is the average current of the inductor.

Equation (3) can be simplified as

$$I_{i4} = I_L d_i, i = 1, 2, 3. \tag{4}$$

Obviously, the current of line i is linearly related to the duty cycle d_i, which means d_i can regulate the power flow of corresponding line.

Substituting (4) into (2), the power conservation equation for the ES-PL is as follows:

$$V_{C1}I_{14} + V_{C2}I_{24} + V_{C3}I_{34} - V_{\text{es}}d_4I_L = 0. \tag{5}$$

In fact, d_4I_L is the average current injecting into ES within a switching cycle, and the average ES power can be written as

$$P_{\text{es}} = V_{C1}I_{14} + V_{C2}I_{24} + V_{C3}I_{34}. \tag{6}$$

In Fig. 3 where ES-PL is applied to the hybrid system, the total power delivered from three dc MGs can be calculated as

$$P_{\text{trans}} = V_{\text{dc1}}I_{14} + V_{\text{dc2}}I_{24} + V_{\text{dc3}}I_{34}. \tag{7}$$

Then the power leverage ratio of ES-PL can be defined as

$$\frac{P_{\text{trans}}}{P_{\text{es}}} = \frac{V_{\text{dc1}}I_{14} + V_{\text{dc2}}I_{24} + V_{\text{dc3}}I_{34}}{V_{C1}I_{14} + V_{C2}I_{24} + V_{C3}I_{34}}. \tag{8}$$

Typically, V_{Ci} has the value less than 20% of $V_{\text{dc}i}$. Therefore, it is straightforward to verify that the power leverage ratio given in (8) would always exceed 1. This confirms that the proposed ES-PL functions as a lever in hybrid ac/dc MG communities, enabling a small amount of ES power to influence network power flow by larger magnitudes.

III. Proposed Interplexed GPS Scheme

A. Droop-Dominated AC and DC MGs

Inspired by classic power systems, f_{ac}–P_{ac} and V_{ac}–Q_{ac} droop controllers are implemented in the ac MG [27]. These droop expressions can be written as follows:

$$\begin{aligned} f_{\text{ac}} &= f_{\text{acmax}} - k_{\text{ac}P}P_{\text{ac}}^M \\ V_{\text{ac}} &= V_{\text{acmax}} - k_{\text{ac}Q}Q_{\text{ac}}^M \end{aligned} \tag{9}$$

where f_{acmax} and V_{acmax} are the allowable maximum ac frequency and maximum voltage amplitude, respectively. $K_{\text{ac}P}$ and $K_{\text{ac}Q}$ are the droop coefficients designed as follows:

$$\begin{aligned} k_{\text{ac}P} &= (f_{\text{acmax}} - f_{\text{acmin}})/P_{\text{acmax}} \\ k_{\text{ac}Q} &= (V_{\text{acmax}} - V_{\text{acmin}})/Q_{\text{acmax}} \end{aligned} \tag{10}$$

where P_{acmax} and Q_{acmax} are the active and reactive power ratings of ac MG.

In (9), P_{ac}^M and Q_{ac}^M are measured values processed by low pass filters (LPFs), the expressions of which are

$$P_{\text{ac}}^M = \frac{\omega_L}{s + \omega_L}P_{\text{ac}},\ Q_{\text{ac}}^M = \frac{\omega_L}{s + \omega_L}Q_{\text{ac}} \tag{11}$$

where ω_L is the cutoff frequency of the given LPFs. P_{ac} and Q_{ac} are the real active power and reactive power.

Given that reactive power is only confined in the ac MG and would not exist in the dc part, this article focuses on managing the active power transfer between ac and dc MGs.

The droop controller for dc MGs is much simpler as there exists no f_{ac} and Q_{ac} in dc system. For a main power source in dc MG, its droop controller could be given as follows [28]:

$$V_{\text{dc}i} = V_{\text{dcmax}} - k_{\text{dc}i}P_{\text{dc}i}^M, i = 1, 2, 3 \tag{12}$$

where V_{dcmax} represents the maximum output voltage of the dc MG. $k_{\text{dc}i}$ is the DC droop coefficient designed as follows:

$$k_{\text{dc}i} = (V_{\text{dcmax}} - V_{\text{dcmin}})/P_{\text{dc}i\text{max}} \tag{13}$$

where $P_{\text{dc}i\text{max}}$ is the power rating of dc MGi. Similarly, $P_{\text{dc}i}^M$ is the measured power delivered by a LPF

$$P_{\text{dc}i}^M = \frac{\omega_L}{s + \omega_L}P_{\text{dc}i}. \tag{14}$$

B. Proposed Interplexed GPS Scheme

AC and dc MGs may frequently encounter situations where one MG is overloaded while others are lightly loaded. Therefore, achieving effective power sharing is crucial to mitigate load imbalances and ensure coordinated operation across the hybrid MGs [29]. In this section, the power sharing between dc MGs is first derived. Based on this, the principle of GPS throughout the hybrid ac/dc MGs community is comprehensively established. This principle consistently translates floating dc voltage and ac frequency into a uniform range, allowing for direct comparison between these distinct electrical parameters.

According to the aforementioned droop scheme, the power sharing within the dc MGs can be accomplished by regulating each dc bus voltage to an identical level. The derivation in steady state is as follows, where K represents the ratio of output power to power rating for each dc MG

$$\frac{P_{\text{dc1}}}{P_{\text{dc1max}}} = \frac{P_{\text{dc2}}}{P_{\text{dc2max}}} = \frac{P_{\text{dc3}}}{P_{\text{dc3max}}} = K. \tag{15}$$

Since the following analysis is based on steady states, the dynamics of LPF can be temporarily disregarded. $P_{\text{dc}i}^{M}$ and P_{ac}^{M} can be replaced by $P_{\text{dc}i}$ and P_{ac}. Then (12) can be written as

$$V_{\text{dc}} = V_{\text{dcmax}} - k_{\text{dc}i}P_{\text{dc}i}. \tag{16}$$

Substituting (13), (15), into (16) results in

$$\begin{aligned} V_{\text{dc}i} &= V_{\text{dcmax}} - \frac{(V_{\text{dcmax}} - V_{\text{dcmin}})}{P_{i\text{max}}} P_{\text{dc}i} \\ &= V_{\text{dcmax}} - (V_{\text{max}} - V_{\text{min}}) \times K \end{aligned} \tag{17}$$

then

$$V_{\text{dc1}} = V_{\text{dc2}} = V_{\text{dc3}}. \tag{18}$$

Since these dc MGs share the same output voltage, they can be considered as an equivalent single dc MG to simplify analyses. This dc MG is connected to the ac MG by the proposed ES-PL. Combining droop equations of dc MGs in (16), their collective expression can be written as

$$V_{\text{dc}} = V_{\text{dcmax}} - k_{\text{dc}P}P_{\text{dc}} \tag{19}$$

where $k_{\text{dc}P}$ is the equivalent droop coefficient. P_{dc} is the total power of the dc MGs. They are expressed as follows:

$$k_{\text{dc}P} = \left(\sum_{i=1}^{3} k_{\text{dc}i}^{-1}\right)^{-1}, P_{\text{dc}} = \sum_{i=1}^{3} P_{\text{dc}i}. \tag{20}$$

Substituting (13) into (20) gives

$$k_{\text{dc}P} = \frac{V_{\max} - V_{\min}}{P_{\text{dcmax}}} \tag{21}$$

where P_{dcmax} is the total power rating of the equivalent dc MG, and it is equal to $\sum_{i=1}^{3} P_{\text{dc}i\text{max}}$.

Based on the expression of equivalent dc MG, (19), GPS can be achieved provided that the power sharing between the equivalent dc MG and ac MG is ensured, i.e.,

$$\frac{P_{\text{dc}}}{P_{\text{dcmax}}} = \frac{P_{\text{ac}}}{P_{\text{acmax}}}. \tag{22}$$

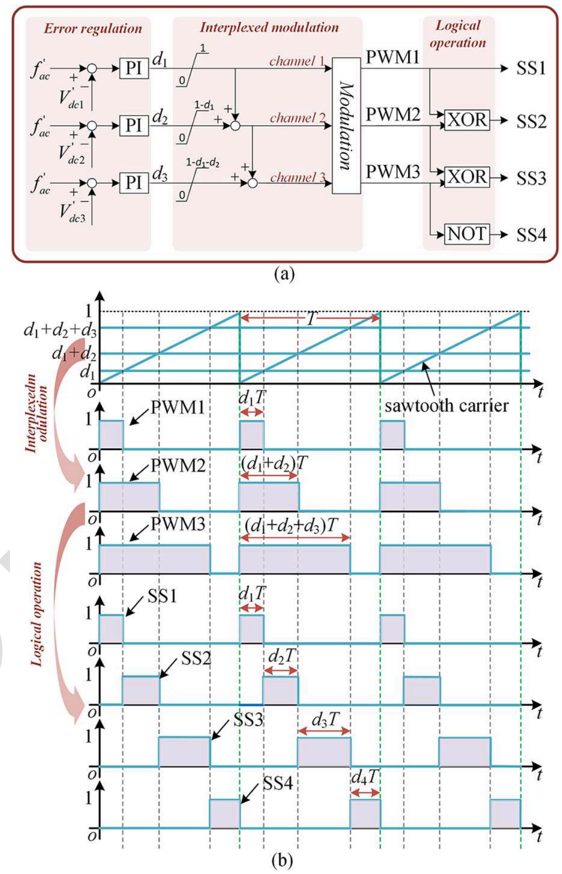

Fig. 5. (a) Interplexed GPS control strategy of ES-PL. (b) Waveforms of interplexed modulation and logical operation.

Substituting (9) and (19) into (22) gives

$$\frac{V_{\text{dcmax}} - V_{\text{dc}}}{k_{\text{dc}P}P_{\text{dcmax}}} = \frac{f_{\text{acmax}} - f_{\text{ac}}}{k_{\text{ac}P}P_{\text{acmax}}}. \tag{23}$$

Substituting (10) and (21) into (23) results in

$$\frac{V_{\text{dcmax}} - V_{\text{dc}}}{V_{\text{dcmax}} - V_{\text{dcmin}}} = \frac{f_{\text{acmax}} - f_{\text{ac}}}{f_{\text{acmax}} - f_{\text{acmin}}}. \tag{24}$$

Equation (24) is the normalization of voltage and frequency. Considering (18), set the normalized formats for each MG as below

$$V_{\text{dc}i}^{'} = \frac{V_{\text{dcmax}} - V_{\text{dc}i}}{V_{\text{dcmax}} - V_{\text{dcmin}}}, f_{\text{ac}}^{'} = \frac{f_{\text{acmax}} - f_{\text{ac}}}{f_{\text{acmax}} - f_{\text{acmin}}}. \tag{25}$$

Then the equivalent condition of GPS is to equalize $f_{\text{ac}}^{'}$ and $V_{\text{dc}i}^{'}$. Based on (25), a novel interplexed GPS control strategy is designed, as shown in Fig. 5(a). This strategy can be divided into three stages: error regulation, interplexed modulation, and logical operation, respectively. In the error regulation stage, the difference between $f_{\text{ac}}^{'}$ and $V_{\text{dc}i}^{'}$ is fed into a PI controller to produce the duty cycle for ES-PL.

For the interplexed modulation stage, the upper limit of d_2 is determined by d_1, while the upper limit of d_3 is constrained by both d_1 and d_2. The duty cycle from channel 1 is first superposed onto the signal in channel 2. The combined result is further added to the signal in channel 3. This interplex of cross-channel

TABLE I
SYSTEM PARAMETERS

Parameters	Description	Value
f_{acmax}	Maximum ac frequency	51 Hz
f_{acmin}	Minimum ac frequency	49 Hz
V_{dcmax}	Maximum dc bus voltage	710 V
V_{dcmin}	Minimum dc bus voltage	705 V
V_{dc4}	dc bus 4 voltage	700 V
P_{acmax}	ac MG power rating	10 kW
P_{dc1max}	dc MG1 power rating	12 kW
P_{dc2max}	dc MG2 power rating	14 kW
P_{dc3max}	dc MG3 power rating	16 kW
ω_L	Cutoff frequency of LPFs	100 rad/s
R_{line}	Line resistance	0.7 Ω
L_{line}	Line inductance	1 mH
V_{es}	voltage of ES	5 V
L_1, L_2	Inductors of ES-PL	20 mH
C_1, C_2, C_3	Capacitors of ES-PL	20 mF
f_s	Switching frequency of ES-PL	10 kHz
$P_{\text{loaddc}i}$	Local load of dc MG i	5 kW
P_{loadac}	Local load of ac MG	30 kW

control signals ensures that the duty cycle consistently satisfies the requirement specified in (1). These three duty cycles are then compared to sawtooth waves to generate pulse width modulation signals, i.e., PWM1, PWM2, and PWM3. Finally, the logical operation generates switch signals (SSi, $i = 1, 2, 3, 4$), which are allocated to corresponding switches in ith module in Fig. 4. Fig. 5(b) visualizes the process of interplexed modulation and logical operation.

For conventional power flow controllers, the CDoF is normally less than the number of the lines whose power flows are to be adjusted. However, thanks to the modularized design and the integration of ES in the proposed ES-PL, the system CDoF can be equal to the number of power lines linked to the facility, which enables much more flexible power flow regulations in hybrid ac/dc MGs community.

IV. FULL STATE-SPACE MODELING AND KEY CONTROL PARAMETER SELECTION GUIDELINE

In this section, the full state-space model of the hybrid system is developed. By means of the model, analyses of small signal stability and guidelines for selecting key control parameters are provided.

For quantitative interpretations, a specific system is studied, as shown in Fig. 3. Key system parameters and the corresponding descriptions are concluded in Table I. The steady-state equations of the system are analyzed as follows. Set the resistor between dc buses i and j as R_{ij}. The current of line i can be written as follows:

$$(V_{\text{dc}i} - V_{Ci} - V_{\text{dc}4})/R_{i4} = I_{i4}, i = 1, 2, 3. \tag{26}$$

For each dc MG, the output power can be expressed as follows:

$$P_{\text{dc}i} = V_{\text{dc}i} I_{i4} + P_{\text{loaddc}i}, i = 1, 2, 3 \tag{27}$$

where $P_{\text{loaddc}i}$ is the local load of dc MG i.

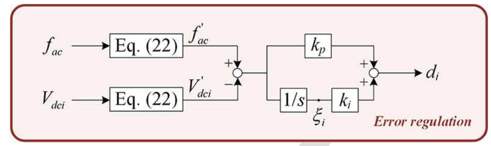

Fig. 6. Error regulation control diagram for the error between f'_{ac} and V'_{dc}.

Considering the power conditions of the entire system, the following expression can be established:

$$P_{\text{dc}} + P_{\text{ac}} + P_{\text{es}} = \sum_{i=1}^{3} P_{\text{loaddc}i} + P_{\text{loadac}} + P_{\text{loss}}. \tag{28}$$

The output power of ES can be expressed as follows:

$$P_{\text{es}} = d_4 V_{\text{es}} I_L. \tag{29}$$

Besides, the power loss can be attributed to the line resistors, of which the expression is

$$P_{\text{loss}} = I_{14}^2 R_{14} + I_{24}^2 R_{24} + I_{34}^2 R_{34}. \tag{30}$$

The system is characterized by 19 steady-state equations, as represented by (1), (4), (5), (9), (12), (18), (23), and (26)–(28). These equations encompass 19 unknown variables: $[V_{\text{dc}1}, V_{\text{dc}2}, V_{\text{dc}3}, f_{\text{ac}}, P_{\text{dc}1}, P_{\text{dc}2}, P_{\text{dc}3}, P_{\text{ac}}, V_{C1}, V_{C2}, V_{C3}, I_L, d_1, d_2, d_3, d_4, I_{14}, I_{24}, I_{34}]$. Therefore, given known load conditions, Newton-Raphson iterative algorithm can uniquely determine the steady state solution of the entire system [30].

A. Full State-Space Modeling of ES-PL

The full state-space model is composed of three parts: MGs, line impedance, and the ES-PL. Set the state vector as follows:

$$\boldsymbol{x} = \begin{bmatrix} \boldsymbol{x}_{\text{MG}} & \boldsymbol{x}_{\text{Line}} & \boldsymbol{x}_{\text{PL}} \end{bmatrix}^T. \tag{31}$$

where

$$\begin{aligned} \boldsymbol{x}_{\text{MG}} &= \begin{bmatrix} v_{\text{dc}1} & v_{\text{dc}2} & v_{\text{dc}3} & f_{\text{ac}} \end{bmatrix}^T \\ \boldsymbol{x}_{\text{Line}} &= \begin{bmatrix} i_{14} & i_{24} & i_{34} & i_{12} & i_{23} \end{bmatrix}^T \\ \boldsymbol{x}_{\text{PL}} &= \begin{bmatrix} v_{C1} & v_{C2} & v_{C3} & i_L & \xi_1 & \xi_2 & \xi_3 \end{bmatrix}^T \end{aligned} \tag{32}$$

where ξ_i is the dynamic of the integral element in the PI controller in ES-PL as shown in Fig. 6.

As for dc MGs, substituting (14) into (12), the dynamic of $V_{\text{dc}i}$ is as follows:

$$\dot{v}_{\text{dc}i} = \omega_L (V_{\text{dc}i\text{max}} - v_{\text{dc}i}) - \omega_L k_{\text{dc}i} p_{\text{dc}i}. \tag{33}$$

Similarly, the dynamic of f_{ac} can be written as

$$\dot{f}_{\text{ac}} = \omega_L (f_{\text{acmax}} - f_{\text{ac}}) - \omega_L k_{\text{ac}P} p_{\text{ac}}. \tag{34}$$

Choosing the state vector $\boldsymbol{x}$ for the whole system and performing small signal disturbances, the linearized dynamic equation of (33) and (34) can be derived as

$$\Delta\dot{\boldsymbol{x}}_{\text{MG}} = \boldsymbol{A}_{\text{MG}} \Delta\boldsymbol{x}_{\text{MG}} + \boldsymbol{A}_{\text{MG,Line}} \Delta\boldsymbol{x}_{\text{Line}} + \boldsymbol{A}_{\text{MG,PL}} \Delta\boldsymbol{x}_{\text{PL}}. \tag{35}$$

For line impedance, their state equations are

$$
\begin{aligned}
L_{j4}\dot{i}_{j4} &= v_{\mathrm{dc}j} - v_{Cj} - v_{\mathrm{dc4}} - i_{j4}R_{j4}, j = 1, 2, 3 \\
L_{12}\dot{i}_{12} &= v_{\mathrm{dc1}} - v_{\mathrm{dc2}} - i_{12}R_{12} \\
L_{23}\dot{i}_{23} &= v_{\mathrm{dc2}} - v_{\mathrm{dc3}} - i_{23}R_{23}
\end{aligned} \tag{36}
$$

where L_{ij} is the line inductor between dc bus i and bus j. Linearizing (36), the small signal model of line impedance can be written as

$$
\Delta\dot{\boldsymbol{x}}_{\mathrm{Line}} = \boldsymbol{A}_{\mathrm{Line,MG}}\Delta\boldsymbol{x}_{\mathrm{MG}} + \boldsymbol{A}_{\mathrm{Line}}\Delta\boldsymbol{x}_{\mathrm{Line}} + \boldsymbol{A}_{\mathrm{Line,PL}}\Delta\boldsymbol{x}_{\mathrm{PL}}. \tag{37}
$$

The model of ES-PL can be divided into two parts: components part and control part. As for components part, their state equations are

$$
\begin{aligned}
C_j\dot{v}_{Cj} &= i_{j4} - d_j i_L, j = 1, 2, 3 \\
L\dot{i}_L &= d_1 v_{C1} + d_2 v_{C2} + d_3 v_{C3} - d_4 V_{\mathrm{es}}.
\end{aligned} \tag{38}
$$

As for control part, the dynamic equations of state vectors are obvious

$$
\dot{\xi}_i = f'_{\mathrm{ac}} - V'_{\mathrm{dc}i}, i = 1, 2, 3 \tag{39}
$$

$$
d_i = k_p\dot{\xi}_i + k_i\xi_i \tag{40}
$$

where k_p and k_i are the proportional coefficient and the integral coefficient of PI controllers.

Linearizing (38) and (39) and substituting (40) into v_C, i_L dynamics, the model of ES-PL can be written as

$$
\Delta\dot{\boldsymbol{x}}_{\mathrm{PL}} = \boldsymbol{A}_{\mathrm{PL,MG}}\Delta\boldsymbol{x}_{\mathrm{MG}} + \boldsymbol{A}_{\mathrm{PL,Line}}\Delta\boldsymbol{x}_{\mathrm{Line}} + \boldsymbol{A}_{\mathrm{PL}}\Delta\boldsymbol{x}_{\mathrm{PL}}. \tag{41}
$$

By consolidating the models of MGs, line impedance and ES-PL, the overall small signal dynamic equation is given as

$$
\begin{bmatrix} \Delta\dot{\boldsymbol{x}}_{\mathrm{MG}} \\ \Delta\dot{\boldsymbol{x}}_{\mathrm{Line}} \\ \Delta\dot{\boldsymbol{x}}_{\mathrm{PL}} \end{bmatrix} = \underbrace{\begin{bmatrix} \boldsymbol{A}_{\mathrm{MG}} & \boldsymbol{A}_{\mathrm{MG,Line}} & \boldsymbol{A}_{\mathrm{MG,PL}} \\ \boldsymbol{A}_{\mathrm{Line,MG}} & \boldsymbol{A}_{\mathrm{Line}} & \boldsymbol{A}_{\mathrm{Line,PL}} \\ \boldsymbol{A}_{\mathrm{PL,MG}} & \boldsymbol{A}_{\mathrm{PL,Line}} & \boldsymbol{A}_{\mathrm{PL}} \end{bmatrix}}_{A_{\mathrm{system}}16\times16} \begin{bmatrix} \Delta\boldsymbol{x}_{\mathrm{MG}} \\ \Delta\boldsymbol{x}_{\mathrm{Line}} \\ \Delta\boldsymbol{x}_{\mathrm{PL}} \end{bmatrix}. \tag{42}
$$

Fig. 7(a) shows that main eigenvalues loci of the system described in (38) with k_p increasing from 0.05 to 0.7 with step of 5×10^{-2} while k_i keeps unchanged at 0.5. It is obvious that conjugate eigenvalues have the negative real part when $k_p = 0.6$, which means the MGs community is stable. However, as k_p is set as 0.65, dominant poles pass through the imaginary axis and enter into the right half plane. This indicates the instability of the system. Fig. 7(b) shows that main eigenvalues loci with k_i increasing from 2.5 to 35 with step of 2.5 under $k_p = 0.005$. It can be observed that the system becomes unstable when k_i is set as 35. All these findings are validated in the subsequent simulations.

Fig. 8 illustrates the simulation results, with dc MGs voltages serving as the stability indicator. Fig. 8(a) shows the validation of k_p impacts on system stability. From the very beginning, ES-PL is commissioned and entire hybrid ac/dc MGs community is stable with k_p selected as 0.6. At 1 s, increasing k_p from 6×10^{-1} to 6.5×10^{-1} induces system oscillations. Fig. 8(b) demonstrates the validation of k_i. A case with the ES-PL in operation is selected for validation. The system stabilizes at $k_i = 32.5$. When k_i increases to 35, the system exhibits oscillations after the ES-PL is put into operation at 1 second. These observations are consistent with eigenvalue behavior analyses presented earlier.

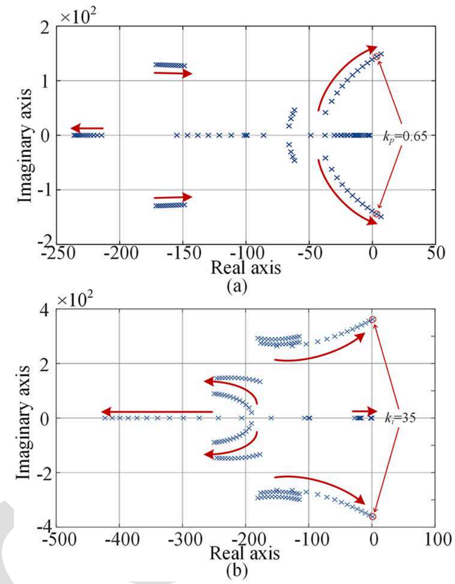

Fig. 7. Eigenvalue loci with control parameter variation with (a) k_p increases from 0.05 to 0.7 with step of 0.05 under $k_i = 0.5$ and (b) k_i increases from 2.5 to 35 with step of 2.5 under $k_p = 0.005$.

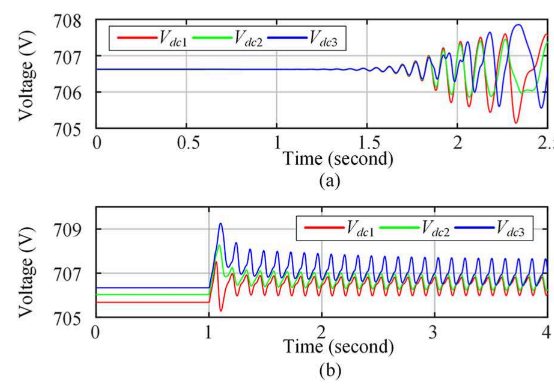

Fig. 8. Simulation verification results with control parameters variation with (a) k_p increasing from 0.6 to 0.65 at 1 second and (b) k_i set as 35 before ES-PL is put into operation.

B. Key Control Parameters Selection Guideline

Based on the earlier small signal analysis of control parameters, an effective method is proposed to guide the optimal selection for these parameters. These guidelines can be summarized into the following three steps.

Step 1: Develop a small signal model of the system and estimate the approximate range based on eigenvalue loci analysis under parameter variations. This step has been conducted in Section IV-A.

Step 2: Shrink the range of parameter selection by investigating into damping ratio.

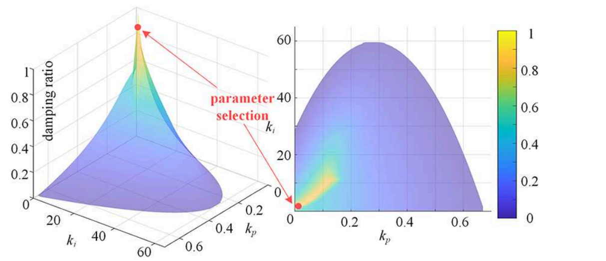

Fig. 9. Stable region of k_p, k_i based on the proposed method. The z-axis denotes to the corresponding damping ratio.

Based on the eigenvalues loci presented in the preceding section, it is evident that the eventual destabilization of the system is attributed to a set of poles crossing the imaginary axis. This set of poles is selected as the focus of study in this section. To perform a quantitative analysis, the damping ratio of the system is defined similar to second-order system [31]

$$\zeta = \cos\theta = \frac{|\mathrm{Re}(p)|}{\sqrt{\mathrm{Re}\,(p)^2 + \mathrm{Im}\,(p)^2}} \tag{43}$$

where θ denotes the angle formed by the line connecting this set of poles to the origin. The real axis and $\mathrm{Re}\,(p)$ and $\mathrm{Im}\,(p)$ represent the real and imaginary parts of these poles, respectively.

Based on this definition, the damping ratio of the system within the stable region of k_p and k_i can be obtained (see Fig. 9). Naturally, low damping ratio means that the system is more prone to oscillation. Therefore, the range of k_p, k_i selection can be narrowed down to the region with high damping ratio, which corresponds to the yellow area in Fig. 9.

Step 3: Identify optimal parameter values through comparative simulations.

Based on the aforementioned narrowed range, the next step is to determine the parameters through comparative simulations. Two cases are given in this part to justify the choice of specific parameters by comparison. In the simulations, ES-PL has been dispatched into operation. The load conditions are as follows: $P_{\mathrm{loaddc1}} = 5$ kW, $P_{\mathrm{loaddc2}} = 5$ kW, $P_{\mathrm{loaddc3}} = 5$ kW, and $P_{\mathrm{loadac}} = 20$ kW. The load of ac MG side is jumped from 20 kW to 15 kW at 1 s.

1) k_p selection: Fig. 10 shows the transient process of dc MGs bus voltages given this step-down of ac MG load. The value of k_i set as 5×10^{-1} after initial attempts. Fig. 10(a) shows a relatively rapid and smooth transient process. The transient process in Fig. 10(b) exhibits slight oscillations, while Fig. 10(c) shows very pronounced oscillations. Considering the above discussion, the value of k_p is set as 5×10^{-3}.
2) k_i selection: Fig. 11 shows the transient process of dc MGs bus voltages given this step-down of ac MG load. The value of k_p set as $5 \times 10 - 3$ for the analysis of the above case. The rise of voltage in Fig. 11(a) is relatively smooth but slow with a transient process around 4 s. The transient process in Fig. 11(b) is smooth and rapid. The voltages in Fig. 11(c) have a clear overshot and oscillations. Considering the above discussion, the value of k_i is set as 5×10^{-1}.

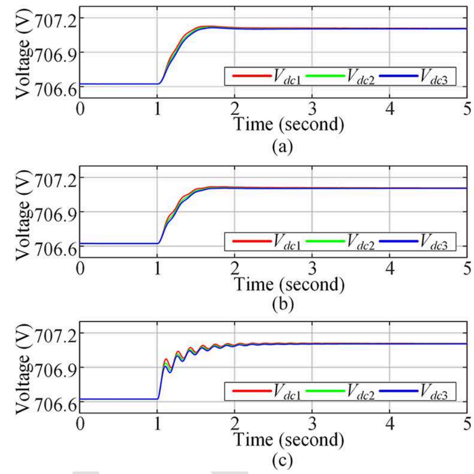

Fig. 10. DC MGs Bus voltage waveforms for different k_p under $k_i = 5 \times 10^{-1}$. (a) $k_p = 5 \times 10^{-3}$. (b) $k_p = 2 \times 10^{-2}$. (c) $k_p = 1 \times 10^{-1}$.

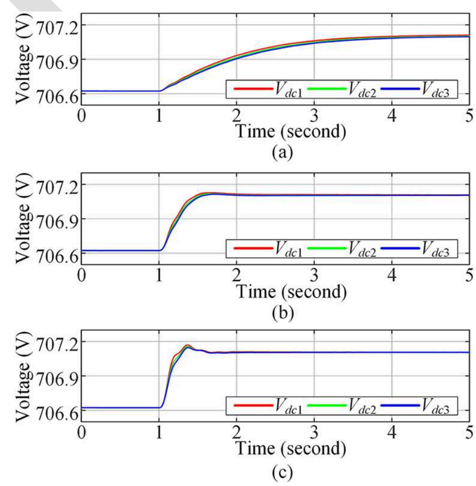

Fig. 11. DC MGs Bus voltage waveforms for different k_i under $k_p = 5 \times 10^{-3}$. (a) $k_i = 1 \times 10^{-1}$. (b) $k_i = 5 \times 10^{-1}$. (c) $k_p = 1$.

V. Discussion

A. Literature Comparisons

This section elaborates on the novelty and advantages of the ES-PL with its interplexed GPS scheme over solid state transformer (SST), energy router, and small-scale flexible ac transmission systems (FACTS). For SST, the topologies in studies regarding SST are all based on FRPS [32], [33], [34], [35], which has been widely demonstrated being less efficient and induced higher capital cost than the proposed ES-PL developed upon PRPS. The topology of energy router in [36] is also falls into FRPS. Besides, focus of the study in [37] is the problem formulation of power flow analyses for hybrid ac/dc MG, whereas in this article, the intention is to transform the interlinking architecture of ac/dc MGs community by proposing

TABLE II
COMPARISONS BETWEEN ES-PL WITH ITS INTERPLEXED GPS SCHEME AND EXISTING METHODS

References	PRPS	Smaller Rating of ES	GPS	Modularized Topology Design	Full State Space Model and Stability Analyses
[11], [12], [13]	✓	×	×	×	-
[14]	✓	×	×	✓	-
[32]	×	×	×	×	✓
[33], [34], [35]	×	×	×	×	×
[36], [37]	×	×	×	×	×
[38], [39], [40], [41]	✓	×	×	×	×
This article	✓	✓	✓	✓	✓

a new type of device, ES-PL. From function point of view, studies regarding small-scale FACTS mainly focus on series–parallel UPQC in ac grid for power quality improvement [38], [39], [40], [41]. Although these devices also originate from PRPS that benefit more efficient operations, they refrain from revealing the insights of extending PRPS to the application of advanced global power management of complex hybrid ac/dc distribution system. Fortunately, in this article, a novel interplexed GPS scheme for hybrid ac/dc MGs community is proposed. Detailed comparisons between the ES-PL with its interplexed GPS scheme in this article and reference papers are conducted, and the corresponding results are summarized in Table II.

B. Protection Strategy

Protection strategy is crucial for the stable operation of MGs community. In current research, dc circuit breakers (DCCBs) are commonly adopted for the protection among MGs community [42]. Based on DCCBs and ES-PL, a detailed explanation of coordinated protection for the MGs community is provided. Taking the line between bus 1 and bus 4 as an example, a DCCB is installed at the line branching out from bus 1 and another DCCB is installed at the line branching out from bus 4. When there is fault happening to the line, the two DCCBs will be triggered and isolate the fault from the system. Then ES-PL can perceive the fault and further switch into an interim fault-tolerant operation mode.

VI. EXPERIMENTAL VERIFICATION

To experimentally validate the feasibility and effectiveness of the proposed ES-PL and interplexed GPS scheme for hybrid ac/dc MGs community, a hardware experimental platform is built up as shown in Fig. 12. The experimental platform operates in islanded mode. The dc sources (Chroma 62100H-600S), interfaced with their respective dc/dc converters, establish the corresponding dc buses characterized by $V-P$ droops. The ac bus is formed in the same way. The voltage of dc bus 4 is regulated by a dc/ac converter interlinked to ac bus. The switch signals of ES-PL are generated from dSPACE 1202. Each bus is loaded by a programmable electronic load (Chroma 63210 Electronic Load). More details of the in-house hardware platform have been summarized in Table I.

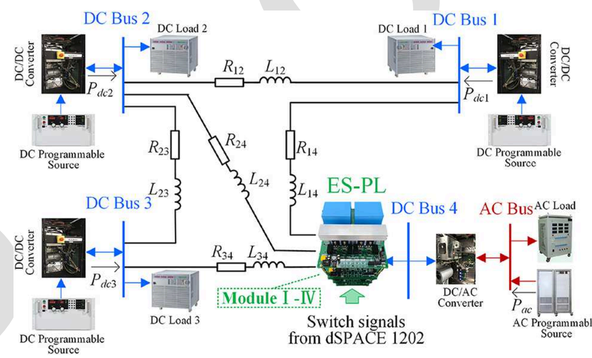

Fig. 12. Hardware experimental platform.

A. Case 1: ES-PL Dispatched into Operation

Fig. 13 demonstrates the scenario that the ES-PL is dispatched into operation. Before the operation of ES-PL, the dc MGs and ac MG are feeding loads of 5 kW and 10 kW, respectively. The voltage of dc bus 4 is maintained by the connected dc/ac converter as 700 V. The programmed ac and dc sources are regulated by their droop schemes. Then the power flow is naturally determined by the difference of voltages between buses. As shown in Fig. 13(a) and (b), the dc MGs all supply power to the ac MG. Consequently, the dc bus voltages approach their lower limits, whereas the ac MG exceeds its frequency upper limits. Once the ES-PL is enabled, the output voltage of dc MGs is raised to the same value which is 707.6 V. The frequency is stabilized at 50 Hz. The GPS among MGs community can be intuitively obtained from Fig. 13(b), where the ratio of the output power of each MG is the same as the ratio of their maximum power ratings in Table I, which is 5 : 6 : 7 : 8. As evident in Fig. 13(c), in this operating condition, the output power of the ES is approximately 40.5 W, and the total power delivered from dc MGs (as defined in Section II) is 5.23 kW. Therefore, the leverage ratio of the proposed ES-PL can be calculated as 129.

B. Case 2: Step-Up of DC MG Load

Following the activation of ES-PL, case 2 examines the system's response to variations in dc side load. In this case, the dc load power, $P_{\mathrm{loaddc}i}$, is set to jump up from 5 to 7 kW to test the stability while P_{loadac} remains 10 kW. Fig. 14 shows the experimental results of case 2. As shown in Fig. 14(a), the voltage of dc buses decrease from 707.6 to 707.0 V and the frequency of ac MG also drops to 49.8 Hz. In Fig. 14(b), as the load demand

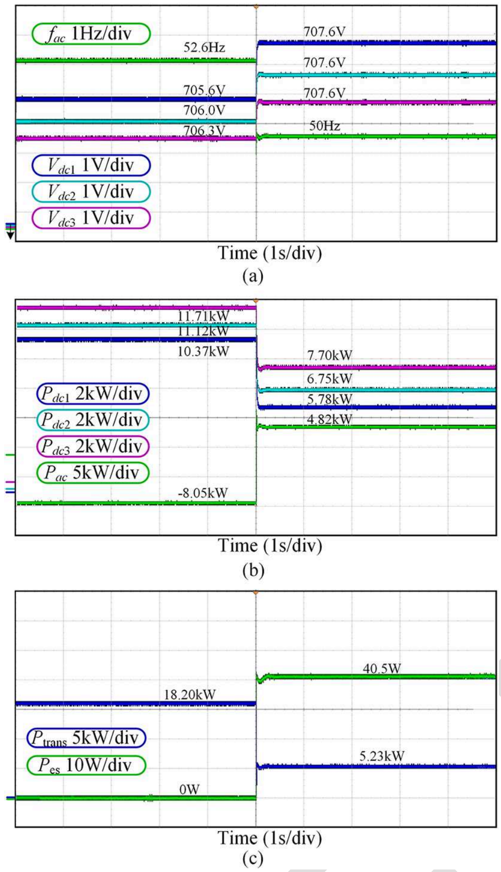

Fig. 13. Experimental results of case 1. (a) $V_{\text{dc}i}$ and f_{ac}. (b) $P_{\text{dc}i}$ and P_{ac}. (c) P_{trans} and P_{es}.

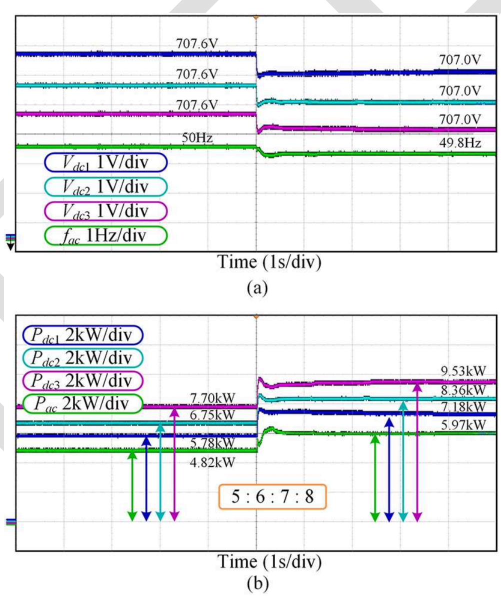

Fig. 14. Experimental results of case 2. (a) $V_{\text{dc}i}$ and f_{ac}. (b) $P_{\text{dc}i}$ and P_{ac}.

rises, all MGs scale their output power accordingly. Notably, the power sharing ratios among MGs remain invariant before and after the load change. This demonstrates the ability of

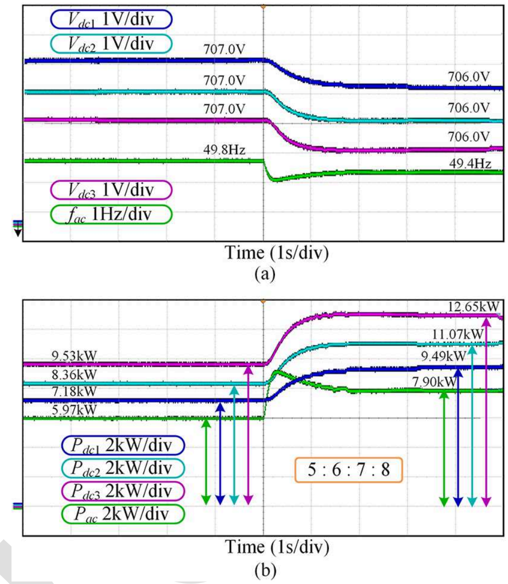

Fig. 15. Experimental results of case 3. (a) V_{dc} and f_{ac}. (b) $P_{\text{dc}i}$ and P_{ac}.

ES-PL to maintain the desired GPS despite the loading changes in DC systems.

C. Case 3: Step-Up of AC MG Load

Fig. 15 illustrates the system dynamics in response to a step increase of ac load. In this case, P_{loadac} is set to jump up from 10 to 20 kW while $P_{\text{load}dci}$ remains constant at 7 kW. As shown in Fig. 15, under the former operating point in case 2, the voltages of three dc buses decline to 706.0 V and ac frequency drops to 49.4 Hz. In spite of the step-up in ac load, the intended GPS ratio across the entire hybrid ac/dc MGs community is still be achieved.

VII. Conclusion

In this article, an ES-PL is proposed for hybrid ac/dc MGs community. The ES-PL by PRPS incorporates ES in a series configuration into the impedance network of the MGs community. Similar to physical levers, the ES system in ES-PL is able to regulate the overall power of the entire system with only a small fraction of its power. This integration additionally introduces an independent CDoF, enabling the ES-PL to actively manage interline power flow. Then the proposed interplexed GPS scheme ensures that all loads are shared among MGs according to their respective ratings. Furthermore, in order to validate the stability of the system, a full state small-signal dynamic model is built and verified through simulations. Based on this model, this article proposes a comprehensive method to guide parameter selection. Comparative studies based on variable operation conditions demonstrate that the proposed ES-PL features lower capital cost and lesser operation loss than FRPS-based ILCs. Finally, hardware experiments are conducted to verify the effectiveness of the proposed architecture. These experiments confirm that the ES-PL effectively utilizes the PRPS for power flow regulation, and that the system remains stable under load variations.

Appendix A
Derivation of the Equivalent Droop Coefficient

As in Section IV-B, an equivalent dc MG is proposed to simplify analyses. The detailed derivation process is as follows.

The droop equations of dc MGs can be written as

$$V_{\mathrm{dc}i} = V_{\mathrm{dcmax}} - k_{\mathrm{dc}i} P_{\mathrm{dc}i}, i = 1, 2, 3. \tag{A1}$$

Divide both sides of the above equation by $k_{\mathrm{dc}i}$

$$\frac{1}{k_{\mathrm{dc}i}} V_{\mathrm{dc}i} = \frac{1}{k_{\mathrm{dc}i}} V_{\mathrm{dcmax}} - P_{\mathrm{dc}i}, i = 1, 2, 3. \tag{A2}$$

According to the derivation of power sharing among dc MGs, the dc bus voltage of each MG is identical

$$V_{\mathrm{dc1}} = V_{\mathrm{dc2}} = V_{\mathrm{dc3}} = V_{\mathrm{dc}}. \tag{A3}$$

Substituting (A2) into (A4)

$$\begin{cases} \frac{1}{k_{\mathrm{dc1}}} V_{\mathrm{dc}} = \frac{1}{k_{\mathrm{dc1}}} V_{\mathrm{dcmax}} - P_{\mathrm{dc1}} \\ \frac{1}{k_{\mathrm{dc2}}} V_{\mathrm{dc}} = \frac{1}{k_{\mathrm{dc2}}} V_{\mathrm{dcmax}} - P_{\mathrm{dc2}} \\ \frac{1}{k_{\mathrm{dc3}}} V_{\mathrm{dc}} = \frac{1}{k_{\mathrm{dc3}}} V_{\mathrm{dcmax}} - P_{\mathrm{dc3}}. \end{cases} \tag{A4}$$

Adding the three equations term by term results in

$$\left(\frac{1}{k_{\mathrm{dc1}}} + \frac{1}{k_{\mathrm{dc2}}} + \frac{1}{k_{\mathrm{dc3}}}\right) V_{\mathrm{dc}} = \left(\frac{1}{k_{\mathrm{dc1}}} + \frac{1}{k_{\mathrm{dc2}}} + \frac{1}{k_{\mathrm{dc3}}}\right) P_{\mathrm{dcmax}} + (P_{\mathrm{dc1}} + P_{\mathrm{dc2}} + P_{\mathrm{dc3}}). \tag{A5}$$

For the equivalent dc MG, the output power is the sum of the output powers of each dc MG

$$P_{\mathrm{dc}} = P_{\mathrm{dc1}} + P_{\mathrm{dc2}} + P_{\mathrm{dc3}}. \tag{A6}$$

Substituting (A6) into (A5)

$$\left(\frac{1}{k_{\mathrm{dc1}}} + \frac{1}{k_{\mathrm{dc2}}} + \frac{1}{k_{\mathrm{dc3}}}\right) V_{\mathrm{dc}} = \left(\frac{1}{k_{\mathrm{dc1}}} + \frac{1}{k_{\mathrm{dc2}}} + \frac{1}{k_{\mathrm{dc3}}}\right) P_{\mathrm{dcmax}} + P_{\mathrm{dc}}. \tag{A7}$$

Divide both sides of the above equation by $(1/k_{\mathrm{dc1}}) + (1/k_{\mathrm{dc2}}) + (1/k_{\mathrm{dc3}})$, the droop expression of the equivalent dc MG can be written as

$$V_{\mathrm{dc}} = P_{\mathrm{dcmax}} + \frac{1}{\frac{1}{k_{\mathrm{dc1}}} + \frac{1}{k_{\mathrm{dc2}}} + \frac{1}{k_{\mathrm{dc3}}}} P_{\mathrm{dc}} \tag{A8}$$

Then the equivalent droop coefficient can be written as

$$k_{\mathrm{dc}P} = \frac{1}{\frac{1}{k_{\mathrm{dc1}}} + \frac{1}{k_{\mathrm{dc2}}} + \frac{1}{k_{\mathrm{dc3}}}} = \left(\sum_{i=1}^{3} k_{\mathrm{dc}i}^{-1}\right)^{-1}. \tag{A9}$$

Considering that different dc MGs may have inconsistent droop coefficients, if the droop coefficients are identical, then according to (A9), it can indeed be derived that the equivalent droop coefficient would be one-third of the original coefficient instead of the sum of the coefficients.

Appendix B
Advantages of ES-PL in Cost and Operation Loss

The following content elaborates on two advantages of the proposed ES-PL based on PRPS over conventional ILCs derived from FRPS, from the perspective of capital cost and loss.

For fair comparisons, three ILCs should be implemented in lines 1, 2, and 3 in the same networked MGs community as shown in Fig. 3, and a four-switch buck-boost topology in [43] is selected for the ILCs in this article. The corresponding tests are also conducted against the same operating conditions and to achieve the same GPS control objective.

A. Cost Comparison Between ES-PL and ILC

The analysis of capital cost is based on the power capacity of the ES-PL and ILCs. According to the electrical characterization of ES-PL, its capacity is determined by the sum of port power on the ES-PL, while the capacity of ILCs is determined by the sum of possible maximum power carried by them. Without the loss of generality, the expressions of carrying power of ILCs and the proposed ES-PL are as follows:

$$\begin{aligned} P_{\mathrm{ILCs}} &= |V_{\mathrm{in1}} I_{14}| + |V_{\mathrm{in2}} I_{24}| + |V_{\mathrm{in3}} I_{34}| \\ P_{\text{ES-PL}} &= |V_{C1} I_{14}| + |V_{C2} I_{24}| + |V_{C3} I_{34}| + |d_4 V_{\mathrm{es}} I_L| \end{aligned} \tag{B1}$$

where $V_{\mathrm{in}i}$ is the input voltage of the ILC in line i.

Fig. B1 illustrates the comparison of the power between ES-PL and ILCs under load variations. The typical operating point is set as: $P_{\mathrm{loaddc1}} = 5$ kW, $P_{\mathrm{loaddc2}} = 5$ kW, $P_{\mathrm{loaddc3}} = 5$ kW, $P_{\mathrm{loadac}} = 10$ kW. As shown in Fig. B1, under variable load conditions, the maximum carrying power of ILCs and ES-PL reaches 30 and 0.4 kW, respectively. Therefore, the rated capacities can be set to 36 kW for ILCs and 0.48 kW for ES-PL, given a 20% design margin. Based on the cost of a 2.2 kW converter in the authors' laboratory, which is 138 \$, a rough estimation can be made that the cost per 1 kW of converter is approximately 63 \$. Then the cost of ILCs and ES-PL can be estimated as 2268 \$ and 30.24 \$. According to industry reports from BLABATT [44], the cost of ES ranges from approximately 200 \$–400 \$ per kWh. This storage capacity is sufficient for the 0.48 kW ES-PL requirements. Therefore, even when including ES costs, the ES-PL maintains a significant economic advantage over the ILCs approach. This comparison result demonstrates that the ES-PL requires a smaller capital cost under the same operating conditions.

B. Operation Loss Comparison Between ES-PL and ILCs

For the aforementioned typical operating condition, the electrical quantities in ES-PL can be computed as: $V_{C1} = 4.4\mathrm{V}, V_{C2} = 3.2\mathrm{V}, V_{C3} = 1.9\mathrm{V}$. According to Fig. 1, the switches in ES-PL should be rated for V_{Ci}. While the switches in ILCs need to withstand $V_{\mathrm{dc}i}$. Specifically, the selection of switches for two converters is detailed in Table B1. For the buck-boost converter-based ILC, two sets of power

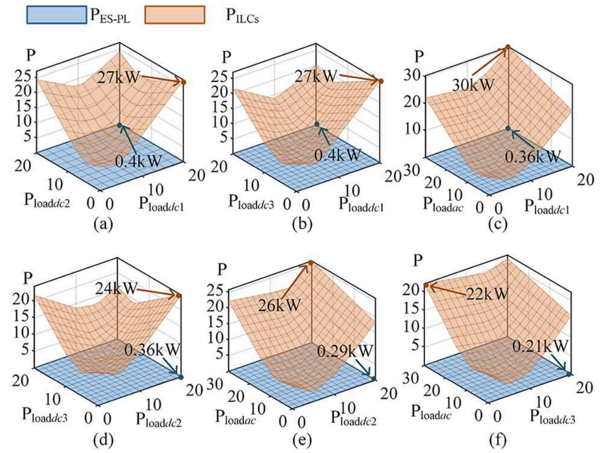

Fig. 16. Comparison of the carrying power of ILCs and ES-PL under identical load variations. The units for all coordinate axes in this figure are kW. (a) Ranges of P_{loaddc1} and P_{loaddc2} are from 0 to 20 kW, when $P_{\text{loaddc3}} = 5$ kW, $P_{\text{loadac}} = 10$ kW. (b) Ranges of P_{loaddc1} and P_{loaddc3} is from 0 to 20 kW, when $P_{\text{loaddc2}} = 5$ kW, $P_{\text{loadac}} = 10$ kW. (c) Range of P_{loaddc1} is from 0 to 20 kW and P_{loadac} is from 0 to 30 kW, when $P_{\text{loaddc2}} = 5$ kW, $P_{\text{loaddc3}} = 5$ kW. (d) Ranges of P_{loaddc2} and P_{loaddc3} are from 0 to 20 kW, when $P_{\text{loaddc1}} = 5$ kW, $P_{\text{loadac}} = 10$ kW. (e) Range of P_{loaddc2} is from 0 to 20 kW and P_{loadac} is from 0 to 30 kW, when $P_{\text{loaddc1}} = 5$ kW, $P_{\text{loaddc3}} = 5$ kW. (f) Range of P_{loaddc3} is from 0 to 20 kW and P_{loadac} is from 0 to 30 kW, when $P_{\text{loaddc1}} = 5$ kW, $P_{\text{loaddc2}} = 10$ kW.

TABLE III
OUT-OF-SHELF COMPONENT SELECTION

	ILCs by FRPS	ES-PL by PRPS
Bbrand	Infineon	Infineon
Model	IRFPG30PBF	IRFZ44NPbF
Drain-source voltage	1000 V	55 V
On-resistance (R_{on})	5 Ω	17.5 mΩ
Rise and fall time (t_r, t_f)	24 ns, 29 ns	60 ns, 45 ns

switches are complementarily turned on [43]. Therefore, as understood from [15], the loss of ILCs can be calculated

$$P_{\text{Loss,ILCs}} = \sum_{1}^{3} (2I_{i4}^2 R_{\text{on1}} + V_{\text{ini}} I_{i4}(t_{r1} + t_{f1}) f_s/2) \quad \text{(B2)}$$

where R_{on1}, t_{r1}, and t_{f1} denote on-resistance, rise time, and fall time of the corresponding switches in ILCs. V_{ini} is the reverse blocking voltage of power switch during turn-off.

According to the electrical characterizations of ES-PL, the turn-on time of each switch within module i during a switching cycle accounts for d_i. Hence, the expression of loss can be calculated

$$P_{\text{Loss,ES-PL}} = \sum_{i=1}^{4} \left(d_i I_L^2 R_{\text{on2}} + V_{\text{ds}i} I_L (t_{r2} + t_{f2}) f_s/2 \right) \quad \text{(B3)}$$

where R_{on2}, t_{r2}, and t_{f2} denote on-resistance, rise time, and fall time of the corresponding switches in ES-PL. $V_{\text{ds}i}$ is the reverse blocking voltage of power switch of module i during turn-off.

Fig. B2 visualizes the comparative results of loss derived from (B2) and (B3). At the aforementioned operating point, the loss of ILCs and ES-PLs is 231 and 14 W, respectively. This

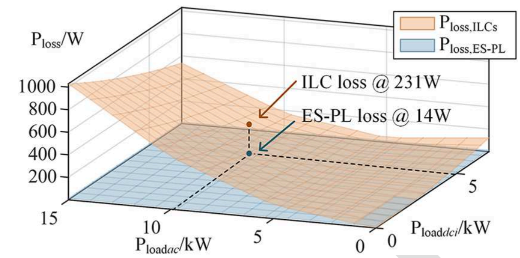

Fig. 17. The comparison of loss between ILCs and ES-PL under identical load conditions. The range of $P_{\text{loaddc}i}$ is from 0 to 7 kW. The range of P_{loadac} is from 0 to 15 kW.

figure shows the FRPS-based ILC induces power loss much higher than the PRPS-based ES-PL.

REFERENCES

[1] J. Duan, Z. Li, Y. Zhou, and Z. Wei, "Study on the voltage level sequence of future urban dc distribution network in China: A review," *Int. J. Electr. Power Energy Syst.*, vol. 117, 2020, Art. no. 105640. AQ5

[2] X. Hou, K. Sun, N. Zhang, F. Teng, X. Zhang, and T. C. Green, "Priority-driven self-optimizing power control scheme for interlinking converters of hybrid AC/DC microgrid clusters in decentralized manner," *IEEE Trans. Power Electron.*, vol. 37, no. 5, pp. 5970–5983, May 2022.

[3] Energy Research Institute @ NTU "Renewable energy integration demonstrator–Singapore," 2022. [Online]. Available: https://www.ntu.edu.sg/erian/research-capabilities/renewable-energy-integration-demonstrator--singapore

[4] P. Lin et al., "A distributed power management strategy for multi-paralleled bidirectional interlinking converters in hybrid AC/DC microgrids," *IEEE Trans. Smart Grid*, vol. 10, no. 5, pp. 5696–5711, Sep. 2019.

[5] P. Lin, T. Zhao, B. Wang, Y. Wang, and P. Wang, "A semi-consensus strategy toward multi-functional hybrid energy storage system in DC microgrids," *IEEE Trans. Energy Convers.*, vol. 35, no. 1, pp. 336–346, Mar. 2020.

[6] P. Lin, Q. Meng, M. Zhu, A. M. Y. M. Ghias, and F. Blaabjerg, "Dynamic circuit-based unified power regulation for hybrid ac/dc/ds microgrids: A comprehensive approach to static and transient control," *IEEE Trans. Ind. Electron.*, early access, Sep. 9, 2025, doi: 10.1109/TIE.2025.3585029.

[7] T. Su, J. Zhao, A. Gomez-Exposito, Y. Chen, V. Terzija, and J. P. Gentle, "Grid-enhancing technologies for clean energy systems," *Nature Rev. Clean Technol.*, vol. 1, no. 1, pp. 16–31, 2025.

[8] P. Wang, C. Jin, D. Zhu, Y. Tang, P. C. Loh, and F. H. Choo, "Distributed control for autonomous operation of a three-port AC/DC/DS hybrid microgrid," *IEEE Trans. Ind. Electron.*, vol. 62, no. 2, pp. 1279–1290, Feb. 2015.

[9] J. Wang, C. Jin, and P. Wang, "A uniform control strategy for the interlinking converter in hierarchical controlled hybrid AC/DC microgrids," *IEEE Trans. Ind. Electron.*, vol. 65, no. 8, pp. 6188–6197, Aug. 2018.

[10] J. Wang, C. Dong, C. Jin, P. Lin, and P. Wang, "Distributed uniform control for parallel bidirectional interlinking converters for resilient operation of hybrid AC/DC microgrid," *IEEE Trans. Sustain. Energy*, vol. 13, no. 1, pp. 3–13, Jan. 2022.

[11] P. Purgat, N. H. van der Blij, Z. Qin, and P. Bauer, "Partially rated power flow control converter modeling for low-voltage DC grids," *IEEE Trans. Emerg. Sel. Topics Power Electron.*, vol. 8, no. 3, pp. 2430–2444, Sep. 2020.

[12] H. Zhang et al., "A partially rated interlinking converter with distributed energy storage for active power sharing in DC microgrids," *IEEE Trans. Power Electron.*, vol. 40, no. 7, pp. 9370–9387, Jul. 2025.

[13] N. G. F. d Santos, J. R. R. Zientarski, and M. L. da Silva Martins, "A two-switch forward partial power converter for step-up/down string PV systems," *IEEE Trans. Power Electron.*, vol. 37, no. 6, pp. 6247–6252, Jun. 2022.

[14] Y. D. Kwon, F. D. Freijedo, T. Wijekoon, and M. Liserre, "A multiport partial power converter for smart home applications," *IEEE Trans. Power Electron.*, vol. 39, no. 7, pp. 8824–8833, Jul. 2024.

[15] R. W. Erickson and D. Maksimovic, *Fundamentals of Power Electronics.* AQ6 Springer Science & Business Media, 2007.

[16] C. Tuo et al., "Decoupling and phase shift control method of modular interline dc power flow controller," *IEEE Trans. Power Del.*, vol. 39, no. 1, pp. 661–674, Feb. 2024.

[17] D. Cheng and J. Zou, "An expandable interline dc power-flow controller," in *Proc. IEEE 3rd Conf. Energy Internet Energy Syst. Integration (EI2)*, Changsha, China, Nov. 2019, pp. 1720–1725.

[18] W. Chen, X. Zhu, L. Yao, X. Ruan, Z. Wang, and Y. Cao, "An interline dc power-flow controller (IDCPFC) for multiterminal HVDC system," *IEEE Trans. Power Del.*, vol. 30, no. 4, pp. 2027–2036, Aug. 2015.

[19] W. Chen et al., "A novel interline DC power-flow controller (IDCPFC) for meshed HVDC grids," *IEEE Trans. Power Del.*, vol. 31, no. 4, pp. 1719–1727, Aug. 2016.

[20] Y. Ye, X. Zhang, Q. Peng, X. Qiu, and X. Yang, "A modular interline power flow controller for meshed multiterminal DC grids," *IEEE Trans. Power Electron.*, vol. 39, no. 8, pp. 10339–10350, Aug. 2024.

[21] H. Zhang et al., "Modular multi-level multi-line DC power flow controller for meshed HVDC grids enabled by decentralized power exchange mechanism," *IEEE Trans. Ind Appl.*, early access Aug. 29, 2025, doi: 10.1109/TIA.2025.3603756.

[22] X. Zhong, M. Zhu, Y. Chi, S. Liu, and X. Cai, "Composite dc power flow controller," *IEEE Trans. Power Electron.*, vol. 35, no. 4, pp. 3530–3542, Apr. 2020.

[23] P. Kundur, "Power system stability," in *Power System Stability and* AQ7 *Control*, 2007, vol. 10, pp. 7–1.

[24] B. Mohandes, M. S. E. Moursi, N. Hatziargyriou, and S. E. Khatib, "A review of power system flexibility with high penetration of renewables," *IEEE Trans. Power Syst.*, vol. 34, no. 4, pp. 3140–3155, Jul. 2019.

[25] H. Hajebrahimi, S. M. Kaviri, S. Eren, and A. Bakhshai, "A new energy management control method for energy storage systems in microgrids," *IEEE Trans. Power Electron.*, vol. 35, no. 11, pp. 11612–11624, Nov. 2020.

[26] S. Huang, Z. Chen, X. Wang, S. Li, X. Yu, and Q. Li, "Performance-guaranteed finite-time secondary control for islanded ac microgrids with time-varying disturbances," *IEEE Trans. Smart Grid*, vol. 16, no. 2, pp. 916–928, Mar. 2025.

[27] R. A. Jabr, "Economic operation of droop-controlled ac microgrids," *IEEE Trans. Power Syst.*, vol. 37, no. 4, pp. 3119–3128, Jul. 2022.

[28] X. Li et al., "Observer-based DC voltage droop and current feed-forward control of a DC microgrid," *IEEE Trans. Smart Grid*, vol. 9, no. 5, pp. 5207–5216, Sep. 2018.

[29] R. Razi, H. Iman-Eini, M. Hamzeh, and S. Bacha, "A novel extended impedance-power droop for accurate active and reactive power sharing in a multi-bus microgrid with complex impedances," *IEEE Trans. Smart Grid*, vol. 11, no. 5, pp. 3795–3804, Sep. 2020.

[30] A. Gil, J. Segura, and N. M. Temme, *Numerical Methods for Special Functions.* Philadelphia, PA, USA: SIAM, 2007.

[31] Z. Lin, W. Huang, R. Li, N. Tai, and J. Liu, "Adaptive damping ratio control of parallel buck converters for the marine pulsed power loads," *IEEE Trans. Power Electron.*, vol. 39, no. 9, pp. 10989–11006, Sep. 2024.

[32] X. Yu, X. She, X. Zhou, and A. Q. Huang, "Power management for dc microgrid enabled by solid-state transformer," *IEEE Trans. Smart Grid*, vol. 5, no. 2, pp. 954–965, Mar. 2013.

[33] C. Kumar, Z. Zou, and M. Liserre, "Smart transformer-based hybrid grid loads support in partial disconnection of MV/HV power system," in *Proc. IEEE Energy Convers. Congr. Expo. (ECCE)*, Milwaukee, WI, USA, Sep. 18–22, 2016, pp. 1–8.

[34] W. A. Rodrigues, R. Santana, A. P. L. Cota, T. Oliveira, L. Morais, and P. Cortizo, "Integration of solid state transformer with DC microgrid system," in *Proc. IEEE 2nd Ann. Southern Power Electronics Conf. (SPEC)*, Auckland, New Zealand, Dec. 5–8, 2016, pp. 1–6.

[35] X. She, A. Q. Huang, S. Lukic, and M. E. Baran, "On integration of solid-state transformer with zonal DC microgrid," *IEEE Trans. Smart Grid*, vol. 3, no. 2, pp. 975–985, Jun. 2012.

[36] Y. Liu, Y. Fang, and J. Li, "Interconnecting microgrids via the energy router with smart energy management," *Energies*, vol. 10, no. 9, 2017, Art. no. 1297.

[37] A. Eajal, M. A. Abdelwahed, E. El-Saadany, and K. Ponnambalam, "A unified approach to the power flow analysis of AC/DC hybrid microgrids," *IEEE Trans. Sustain. Energy*, vol. 7, no. 3, pp. 1145–1158, Jul. 2016.

[38] F. Wang, J. L. Duarte, and M. A. Hendrix, "Grid-interfacing converter systems with enhanced voltage quality for microgrid application—Concept and implementation," *IEEE Trans. Power Electron.*, vol. 26, no. 12, pp. 3501–3513, Dec. 2011.

[39] H. Toodeji, S. Fathi, and G. Gharehpetian, "Power management and performance improvement in integrated system of variable speed wind turbine and UPQC," in *Proc. Int. Conf. Clean Electrical Power*, Capri, Italy, Jun. 9–11, 2009, pp. 609–614.

[40] P. G. Khorasani, M. Joorabian, and S. G. Seifossadat, "Smart grid realization with introducing unified power quality conditioner integrated with dc microgrid," *Electr. Power Syst. Res.*, vol. 151, pp. 68–85, 2017.

[41] M. Zolfaghari, M. Abedi, and G. B. Gharehpetian, "Power flow control of interconnected AC–DC microgrids in grid-connected hybrid microgrids using modified UIPC," *IEEE Trans. Smart Grid*, vol. 10, no. 6, pp. 6298–6307, Nov. 2019.

[42] R. Rodrigues, Y. Du, A. Antoniazzi, and P. Cairoli, "A review of solid-state circuit breakers," *IEEE Trans. Power Electron.*, vol. 36, no. 1, pp. 364–377, Jan. 2021.

[43] J.-J. Chen, P.-N. Shen, and Y.-S. Hwang, "A high-efficiency positive buck–boost converter with mode-select circuit and feed-forward techniques," *IEEE Trans. Power Electron.*, vol. 28, no. 9, pp. 4240–4247, Sep. 2013.

[44] BSLBATT, "What is the current average cost of energy storage systems in 2025." Accessed: Aug. 9, 2025. [Online]. Available: https://bslbatt.com/blogs/current-average-energy-storage-cost-2025/